29 MAR 1999

Solution of the Navier-Stokes Equations in Three Dimensions Using a Fully Unfactored Method

F. Cantariti,M. Woodgate, K. Badcock and B. Richards
Aerospace Engineering Report 9908

Aerospace Engineering Department, University of Glasgow, Glasgow G12 8QQ, U.K.

Engineering
PERIODICALS
U5000

Abstract

An unfactored implicit time-marching method for the solution of the three dimensional Navier-Stokes equations on multiblock curvilinear grids is presented. For robustness the convective terms are discretised using an upwind TVD scheme. A centred approach is followed for the discretisation of the viscous terms. The linear system arising from each implicit time step is solved using a Krylov subspace method with preconditioning based on an block incomplete lower-upper (BILU(0)) factorisation. Results are shown for the ONERA B1 ogive, for the ONERA M6 wing, the NLR-F5 clean wing and the ONERA B2 ogive, demonstrating good comparison with experiment except for some discrepancies in the last case due to turbulence modelling.

1 Introduction

Due to the availability of increased computing power and the advances in numerical methods, computational fluid dynamics (CFD), is becoming an important tool for analysing the aerodynamics of aircraft [20]. Opportunities are opening up for the use of CFD to reduce design cycle costs, evaluate experimental inaccuracies (eg tunnel interference) and provide high resolution information to aid the understanding of flow physics. The most demanding problems for aircraft are experienced in the transonic and supersonic regimes where the minimum level of modelling to satisfactorally model shock waves is the Euler equations. For the separated flow often encountered in practical aircraft, rotorcraft and missile flight, and the interest in maintaining attached flow, the modelling of viscous effects is important. The issue of turbulence modelling is not considered here.

Navier-Stokes solvers for complex aircraft shapes have been used for a number of years. Geometric complexity is tackled through the use of either unstructured or block structured grids. The former have the advantage of grid generation with less human intervention. However, flow codes on unstructured grids require more memory and are generally less efficient. Whilst for simulation of one-off shapes the large cost of the reduced cost of the grid generation stage means that unstructured grids are normally preferred for Euler calculations, for multidisciplinary work such as optimisation,where repetitive calculations on the same grid are required, the emphasis shifts to flow code efficiency and block structured grids are attractive.

The current report describes the development of an implicit method for solving the three dimensional steady state Navier-Stokes equations. This work builds on developments in two dimensions. The features of the method are an iterative solution [6] of an unfactored linear system for the flow updates [3], approximate Jacobian matrices [8] and a preconditioning strategy designed to provide good parallel performance [4]. Applications of the method for steady state problems include for aerofoil flows [3] [8], multielement aerofoils [2], axisymmetric slender body shapes [1] and shock wave reflections in jets [5].

The report continues with a description of the Navier-Stokes equations, followed by the numerical method. Results are then presented for a variet of test cases to illustrate the method performance. Comparison with experimental data is made where available and computing times are given to illustrate the performance of the method.

2 Three-Dimensional Governing Equations

The three-dimensional Cartesian Navier-Stokes equations can be written in non-dimensional conservative form as

$$\frac{\partial \mathbf{W}}{\partial t} + \frac{\partial (\mathbf{F^i} + \mathbf{F^\nu})}{\partial x} + \frac{\partial (\mathbf{G^i} + \mathbf{G^\nu})}{\partial y} + \frac{\partial (\mathbf{H^i} + \mathbf{H^\nu})}{\partial z} = 0 \tag{1}$$

where $\mathbf{W} = (\rho, \rho u, \rho v, \rho w, \rho E)^T$ denotes the vector of conservative variables. The inviscid flux vectors $\mathbf{F^i}$, $\mathbf{G^i}$

and $\mathbf{H^i}$ are,

$$\mathbf{F^i} = \begin{pmatrix} \rho u \\ \rho u^2 + p \\ \rho uv \\ \rho uw \\ u(\rho E + p) \end{pmatrix},$$

$$\mathbf{G^i} = \begin{pmatrix} \rho v \\ \rho uv \\ \rho v^2 + p \\ \rho vw \\ v(\rho E + p) \end{pmatrix},$$

$$\mathbf{H^i} = \begin{pmatrix} \rho w \\ \rho uw \\ \rho vw \\ \rho w^2 + p \\ w(\rho E + p) \end{pmatrix}.$$

In the above ρ, u, v, w, p and ρE denote the density, the three Cartesian components of the velocity, the pressure and the specific total energy respectively. The viscous flux vectors $\mathbf{F^\nu}$, $\mathbf{G^\nu}$ and $\mathbf{H^\nu}$ are given by

$$\begin{aligned}
\mathbf{F^\nu} &= (0, \tau_{xx}, \tau_{xy}, \tau_{xz}, u\tau_{xx} + v\tau_{xy} + w\tau_{xz} + q_x)^T, \\
\mathbf{G^\nu} &= (0, \tau_{xy}, \tau_{yy}, \tau_{yz}, u\tau_{xy} + v\tau_{yy} + w\tau_{yz} + q_y)^T, \\
\mathbf{H^\nu} &= (0, \tau_{xz}, \tau_{yz}, \tau_{zz}, u\tau_{xz} + v\tau_{yz} + w\tau_{zz} + q_z)^T,
\end{aligned}$$

where the components of the stress tensor and of the heat flux vector are modeled in the following way:

$$\begin{aligned}
\tau_{xx} &= -(\mu + \mu_t)\left(2\tfrac{\partial u}{\partial x} - \tfrac{2}{3}(\tfrac{\partial u}{\partial x} + \tfrac{\partial v}{\partial y} + \tfrac{\partial w}{\partial z})\right) \\
\tau_{yy} &= -(\mu + \mu_t)\left(2\tfrac{\partial v}{\partial y} - \tfrac{2}{3}(\tfrac{\partial u}{\partial x} + \tfrac{\partial v}{\partial y} + \tfrac{\partial w}{\partial z})\right) \\
\tau_{zz} &= -(\mu + \mu_t)\left(2\tfrac{\partial w}{\partial z} - \tfrac{2}{3}(\tfrac{\partial u}{\partial x} + \tfrac{\partial v}{\partial y} + \tfrac{\partial w}{\partial z})\right) \\
\tau_{xy} &= -(\mu + \mu_t)\left(\tfrac{\partial u}{\partial y} + \tfrac{\partial v}{\partial x}\right) \\
\tau_{xz} &= -(\mu + \mu_t)\left(\tfrac{\partial u}{\partial z} + \tfrac{\partial w}{\partial x}\right) \\
\tau_{yz} &= -(\mu + \mu_t)\left(\tfrac{\partial v}{\partial z} + \tfrac{\partial w}{\partial y}\right) \\
q_x &= -\tfrac{1}{(\gamma-1)M_\infty^2}\left(\tfrac{\mu}{Pr} + \tfrac{\mu_t}{Prt}\right)\tfrac{\partial T}{\partial x} \\
q_y &= -\tfrac{1}{(\gamma-1)M_\infty^2}\left(\tfrac{\mu}{Pr} + \tfrac{\mu_t}{Prt}\right)\tfrac{\partial T}{\partial y} \\
q_z &= -\tfrac{1}{(\gamma-1)M_\infty^2}\left(\tfrac{\mu}{Pr} + \tfrac{\mu_t}{Prt}\right)\tfrac{\partial T}{\partial z}
\end{aligned}$$

The laminar viscosity μ is evaluated using Sutherland's law whilst the turbulent eddy viscosity is given by Baldwin-Lomax algebraic turbulence model [10]. Finally, the various flow quantities are related to each other by the perfect gas relations.

3 Numerical Method

3.1 Spatial Discretisation

The Navier-Stokes equations are discretised on curvilinear multi-block body conforming grids using a cell-centred finite volume method which converts the partial differential equations of (1) into a set of ordinary differential equations which can be written as

$$\frac{d}{dt}(V_{i,j,k}\mathbf{W}_{i,j,k}) = -\mathbf{R}_{i,j,k}(\mathbf{W}). \tag{2}$$

The convective terms are discretised using Osher's upwind scheme [7] for its robustness, accuracy and stability properties. MUSCL variable extrapolation is used to provide second-order accuracy with the Van Albada limiter to prevent spurious oscillations around shock waves. The discretisation of the viscous terms requires the value of some of the flow variables at the edges of each cell, as well as their derivatives. Cell-edge values are approximated by the average of the two adjacent cell-centre values, whilst cell-edge values of the derivatives are obtained using Green's formula applied to an auxiliary cell made of the two halves of the cells surrounding the considered edge. The choice of the auxiliary cell is guided by the need to avoid odd-even point decoupling and to minimise the amount of numerical viscosity introduced in the discretised equations.

3.2 Implicit Unfactored method

The implicit time marching scheme for equation (2) is given by

$$\frac{\mathbf{W}_{i,j,k}^{n+1} - \mathbf{W}_{i,j,k}^{n}}{\Delta t} = -\frac{1}{V_{i,j,k}}\mathbf{R}_{i,j,k}(\mathbf{W}^{n+1}) \tag{3}$$

where the superscript $n+1$ denotes the time level $(n+1)\times\Delta t$. In order to be able to solve equation (3) the term $\mathbf{R}_{i,j,k}(\mathbf{W}^{n+1})$ is linearised with respect to time:

$$\mathbf{R}_{i,j,k}(\mathbf{W}^{n+1}) \approx \mathbf{R}_{i,j,k}(\mathbf{W}^{n}) + \frac{\partial \mathbf{R}_{i,j,k}}{\partial \mathbf{W}_{i,j,k}}\Delta\mathbf{W}_{i,j,k} \tag{4}$$

where $\Delta\mathbf{W}_{i,j,k} = \mathbf{W}_{i,j,k}^{n+1} - \mathbf{W}_{i,j,k}^{n}$. This leads to the following linear system

$$\left[\frac{V_{i,j,k}}{\Delta t}\mathbf{I} + \frac{\partial \mathbf{R}_{i,j,k}}{\partial \mathbf{W}_{i,j,k}}\right]\Delta\mathbf{W}_{i,j,k} = -\mathbf{R}_{i,j,k}(\mathbf{W}^{n}). \tag{5}$$

In the present work, the left hand side of equation (5) is approximated with first order jacobians as in [8]. This reduces the number of terms in the matrix from 825 per cell to 175 which is essential as 3D problems can easily have several million cells. Initial results have indicated that the present method requires 1 MB of memory per 550 nodes. The right hand side of (5) is not changed to maintain second order spatial accuracy. A Krylov subspace algorithm is used to solve the linear system of equation and is preconditioned using a Block Incomplete Lower-Upper factorisation which has the same sparsity pattern as the jacobian matrix (BILU(0)). Furthermore, the BILU(0) factorisation is decoupled between blocks to improve parallel efficiency. This approach does not seem to have a major impact on the effectiveness of the preconditioner as the number of blocks increases [9].

4 Computational Results

4.1 Results for the ONERA B1 Ogive

The first test case considered is a laminar flow around the ONERA B1 ogive [11] at a freestream Mach number of 2, a Reynolds number based on the ogive diameter of 0.16 million and two angles of attack: 0^o and 10^o. The computational grid used contains 65 points along the body in the direction of the flow, 65 points in the direction normal to the wall surface and 65 points in the circumferential direction (half body). A coarser grid was generated by extracting every other points from the fine one. Using grid sequencing and 4 processors on a cluster of Pentium Pro, the method required less than an hour to reduce the L2 norm of the residual by 6.5 and 5 orders for the 0^o and 10^o case, respectively.

Figure 1 compares the pressure coefficient and skin friction distributions for the 0^o case obtained with the present method with the solution of a 2D axisymmetric code which has been extensively validated [12]. The agreement between the two numerical methods is very good, with nearly perfect matching.

For the 10^o problem, the pressure coefficient distributions along the body and at given X/D stations are shown in Figure 2. The angle $\Phi = 0$ corresponds to the windward side of the ogive, whereas the angle $\Phi = 180$ corresponds to the leeward side. Also, note that the scale of the two graphs is not the same. The agreement between computation and experiment is good, except in the region surrounding the vortex ($120 < \Phi < 160$). These discrepancies might be due to the fact that the flow is actually turbulent. Indeed, the experimental report [11] investigates the influence of natural and fixed transition points between laminar and turbulent flow and shows some substantial differences in the flowfield. Nevertheless, the overall trends are correctly captured by the numerical method. The location of the separation lines is show in Figure 3. Again, the predicted main separation line matches well with the experimentally observed one. Finally, an overview of the flowfield at three different X/D stations can be seen in Figure 4.

4.2 Results for the RAE 2822 Infinite Wing

In order to validate the implementation of the Baldwin-Lomax turbulence model, calculations around an RAE 2822 infinite wing were made. A fine C-type grid was generated with 193 points in the streamwise direction, 33 points in the wake, 65 points in the direction normal to the wall and 5 points in the spanwise direction. The spacing of the first node next to the wall was chosen so as to insure a near wall value of y^+ of around one. The outer boundary was located approximately 15 chords away. Again, a coarser grid was generated by removing every other points from the fine grid. In accordance with the experiment [13], transition points from laminar to turbulent flow were fixed at 3% chord.

Two flow conditions were investigated. Case 9 is at a freestream Mach number of 0.73, and angle of attack of 2.79^o and a Reynolds number of 6.5 million. Case 10 is at a freestream Mach number of 0.75, and angle of attack of 2.81^o and a Reynolds number of 6.2 million. The pressure coefficient and skin friction distributions are shown in Figures 5 and 6 for Case 9 and 10, respectively. For Case 9, the agreement between experiment and computation is good, except for the shock strength which is overestimated. For Case 10, the experimental data and computational results agree well on the lower surface and upstream of the shock wave on the upper surface. However, the location of the shock is predicted to aft, its strength is over-estimated and the pressure levels downstream of the shock are incorrect. Also, the predicted flow separates from the shock wave right up to the trailing-edge, whereas experimentally shock-induced separation with reattachment is observed.

However, several authors, such as Rumsey and Vatsa [14], have found a similar level of agreement for Case 9 and 10 using a Baldwin-Lomax turbulence model, with the discrepancies for Case 10 explained by the deficiencies of the turbulence model for separated or close-to-separation flows.

4.3 Results for the ONERA M6 Wing

The next problem considered in this paper is the flow around the ONERA M6 wing [15]. A C-O type grid was generated containing $129 \times 65 \times 65$ points with 97 points wrapped around the wing section, 17 points in the wake and 65 points in the direction normal to the wing. In the spanwise direction, there are 49 points on the wing and 17 points around half of the tip. The spacing of the first node next to the wall was chosen so as to insure a near wall value of y^+ of around one and the outer boundary was located approximately 15 chords away. This level of grid density was felt to be sufficient in view of the results obtained in the previous section and from our experience with 3D inviscid flows [9].

A first calculation was made for a flow at a Mach number of 0.84, an angle of attack of 3.06^o and a Reynolds number of 11.7 million. The experimental pressure coefficient distributions at several spanwise locations are shown in Figure 7 and are compared with the present turbulent results as well as inviscid ones obtained on a similar size grid. The agreement between experiment and simulations is in general good. But, the turbulent calculations are much closer to the experiment than the inviscid results in the shock wave regions. This is particularly true towards the tip of the wing, from $\eta = 0.9$ onwards where the turbulent simulation predicts the correct location and strength of the shock. At the tip however, both methods fail to capture the pressure plateau towards the trailing-edge due to the tip vortex. A similar level of agreement was achieved by Rumsey and Vatsa [14]. An overview of

the flowfield on the wing upper surface is shown in Figure 8 where the lambda shape of the shock is clearly seen.

A second calculation was made at the same Mach and Reynolds numbers, but at a higher angle of 6.06°. The pressure contours on the wing upper surface are shown in Figure 9 and indicates that the turbulent calculation predicts flow separation downstream of the shock towards the tip of the wing. This is confirmed in Figure 10 where the predicted flow is separated from the shock up to the trailing edge from station $\eta = 0.65$ onwards, whereas experimentally, the flow seems to separate from station $\eta = 0.80$ only. The cause of this mis-match can be attributed to the turbulence model which fails to predict firstly, the correct location of the strong secondary shock towards the root of the wing and secondly, the correct pressure levels downstream of the shock from $\eta = 0.65$. At these stations, it is probable that experimentally shock induced flow separation occurs with reattachment or mild separation.

For both cases, the calculation runtime was under 45 minutes to reduce the L2 norm of the residual by just under 3.5 orders using 6 processors on a cluster of Pentium Pro.

4.4 Results for the NLR-F5 Clean Wing

Next, the flow around a NLR-F5 clean wing was investigated. The flow conditions are as follows: the freestream Mach number is 0.896, the angle of attack is 0.497° and the Reynolds number is 5.79 million. The C-O type grid used is similar in size to that for the ONERA M6 wing, except that in the spanwise direction, there are 57 points on the wing and 9 points around half of the tip since the NLR-F5 wing is only 5% thick.

A comparison between the experimental [16] and computational pressure distributions is shown in Figure 11. The agreement between the numerical results and the experimental data is relatively good, with the turbulent solution showing some improvements compared to the inviscid one near the lower surface leading-edge suction peak and around the upper surface pressure plateau. This is in agreement with the findings of several authors [17], [18]. More importantly, the inviscid method predicts the presence of a shock wave on the wing upper surface from root to tip, while in the turbulent solution, the region where a shock is present is in better agreement with the experiment (see Figure 12). Furthermore, towards the tip of the wing, the turbulent method predicts more correctly the location and the strength of the shock wave.

4.5 Results for the ONERA B2 Ogive

The final test case considered in this paper is the flow around the ONERA B2 ogive [11] at a Mach number of 2, a Reynolds number based on the ogive diameter of 1.2 million and two angles of attack: 0° and 10°. The computational grid used contains 65 points along the body in the direction of the flow, 129 points in the direction normal to the wall surface and 33 and 65 points in the circumferential direction for the 0° case (quarter body) and 10° case (half body), respectively. Transition points from laminar to turbulent flow were fixed at 15 % diameter, in accordance with the experiment. The overall runtime of the code was just under 1 hour and 15 minutes on 4 (0° case) and 8 (10° case) processors to reduce the L2 norm of the residual by 6 orders.

For the 0° angle of attack problem, the predicted pressure coefficient and skin friction distributions are compared with the results of a 2D axisymmetric code using a $k - \omega$ turbulence model [12] (see Figure 13). The agreement between the two sets of data is good, although the skin friction levels predicted by the 3D solver are lower than those predicted by the axisymmetric code. The difference is essentially attributed to the different turbulence models used.

Figure 14 shows the stagnation pressure contours at three different station along the body for the 10° case. It can be seen that the method fails to predict the correct shape of the vortex present on the leeward side of the ogive downstream of X/D = 7. This is caused by the fact that the Baldwin-Lomax turbulence model used over-predicts the value of the eddy viscosity in regions where a vortex can be found. Degani and Schiff [19] have introduced a two-way correction to improve results for that kind of flows. The first correction, which deals with the presence of two distinct maxima in the function F is straight forward to implement. However, the second one, which helps in cases where the maxima are close to each other is not easy to address within a multi-block context and was therefore neglected. The results obtained with that partial Degani-Schiff correction are shown in Figure 15 and some improvements can be seen. However, the strength and position of the vortex are not yet correct and the inclusion of the second part in the Degani-Schiff correction should improve results further.

5 Conclusion

An unfactored implicit time-marching method for solving the three dimensional Navier-Stokes equations has been presented in this paper. Results were shown for the ONERA B1 ogive, the ONERA M6 wing, the NLR-F5 clean wing and the ONERA B2 ogive. Good results were obtained for all cases considered, although the last case in particular emphasises the limitation of the Baldwin-Lomax turbulence model.

Acknowledgements

The authors would like to thank Trevor Birch (DERA) and Michael Henshaw (BAe) for making available some of the experimental data. Also, this work has been par-

tially supported BAe contract (SP050104458), Defence and Evaluation Research Agency (DERA) contract FRNI c/107 and EPSRC (GR/K55455).

References

[1] B.J.Gribben, K.J.Badcock, and B.E.Richards, "Application of PMB2D to axisymmetric flows", Aerospace Engineering Report, 12, Glasgow University, Glasgow, UK, 1998.

[2] B.J.Gribben, "Progress Report: Application of the multiblock method in Computational Aerodynamics", Aerospace Engineering Report, 21, Glasgow University, Glasgow, UK, 1996.

[3] K.J.Badcock and S.Porter and B.E.Richards, "Unfactored Multiblock Methods:Part I Initial Method Development", Aerospace Engineering Report, 11, Glasgow University, Glasgow, UK, 1995.

[4] K.J.Badcock, W.S.McMillan, M.A.Woodgate, B.Gribben, S.Porter, and B.E.Richards, "Integration of an implicit multiblock code into a workstation cluster environment", in *Parallel CFD 96*, p. 408. Capri, Italy, 1996.

[5] B.J. Gribben, K.J. Badcock and B.E. Richards. "Shock Reflection Hysteresis in an Underexpanded Jet: a CFD Study". *University of Glasgow, Aero Report 9808*, 1998.

[6] K.J.Badcock, X.Xu and L.Dubuc and B.E.Richards, "Preconditioners for high speed flows in aerospace engineering", *Numerical Methods for Fluid Dynamics V*,Institute for Computational Fluid Dynamics, Oxford, pp287–294,1996

[7] Osher, S. and Chakravarthy, S., "Upwind Schemes and Boundary Conditions with Applications to Euler Equations in General Geometries", *Journal of Computational Physics*, Vol. 50, pp 447-481, 1983.

[8] Cantariti, F., Dubuc, L., Gribben, B., Woodgate, M., Badcock, K. and Richards, B., "Approximate Jacobians for the Solution of the Euler and Navier-Stokes Equations", Department of Aerospace Engineering, Technical Report 97-05, 1997.

[9] Woodgate, M., Cantariti, F., Badcock, K. and Richards, B., "Solution of the Euler Equations in Three Dimensions Using a Fully Unfactored Method", Department of Aerospace Engineering, Technical Report 98-??, 1998. Also, http://www.aero.gla.ac.uk/Research/CFD/Index.html under publications/codes.

[10] Baldwin, B. and Lomax H., "Thin-Layer Approximation and Algebraic Model for Separated Turbulent Flows", AIAA Paper 78-257,1978.

[11] Barberis, D. "Supersonic Vortex Flow Around a Missile Body", Case Number C-5, in "A Selection of Experimental Test Cases for the Validation of CFD Codes", AGARD-AR-303, 1994.

[12] Gribben, B., Badcock, K. and Richards, B., "Application of PMB2D to Axisymmetric Flows", Department of Aerospace Engineering, Technical Report 98-12, 1998. Also, http://www.aero.gla.ac.uk/Research/CFD/Index.html under publications/applications.

[13] Cook, P., McDonald, M. and Firmin, M., "Airfoil RAE 2822 - Pressure Distributions, and Boundary Layer and Wake Measurements", in "Experimental Data Base for Computer Program Assessment", AGARD-AR-138, 1979.

[14] Rumsey, C. and Vatsa, V., "A Comparison of the Predictive Capabilities of Several Turbulence Models Using Upwind and Central-Difference Computer Codes", AIAA Paper 93-0192, 1993.

[15] Schmitt, V. and Charpin, F., "Pressure Distributions on the ONERA-M6-Wing at Transonic Mach Numbers", in "Experimental Data Base for Computer Program Assessment", AGARD-AR-138, 1979.

[16] Tijdeman, H. *et al.*, "Transonic Wind Tunnel Tests on an Oscillating Wing with External Store. Part II: The Clean Wing", NLR TR 78106 U, 1978.

[17] Guruswamy, G. and Goorjian P., "Efficient Algorithm for Unsteady Transonic Aerodynamics of Low-Aspect-Ratio Wings", *Journal of Aircraft*, Vol. 22, No. 3, pp 193-199, 1985.

[18] Obayashi, S., Guruswamy, G. and Goorjian P., "Streamwise Upwind Algorithm for Computing Unsteady Transonic Flows Past Oscillating Wings", *AIAA Journal*, Vol. 29, No. 10, pp 1668-1677, 1990.

[19] Degani, D. and Schiff, L., "Computation of Supersonic Viscous Flows Around Pointed Bodies at large Incidence", AIAA Paper 83-0034, 1983.

[20] Jameson, A. , "The present status, challenges and future developments in computational fluid dynamics", *AGARD symposium on Progress and Challenges in CFD Methods and Algorithms*, Seville, Spain, October 1995.

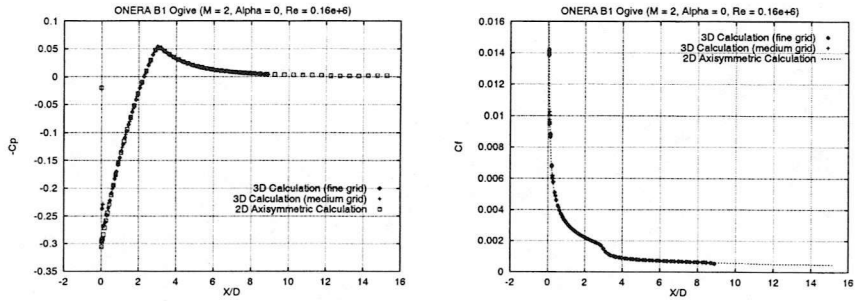

Figure 1: Pressure coefficient and skin friction distributions
ONERA B1 Ogive, $M_\infty = 2$, $\alpha = 0^o$, Re = 0.16 10^6

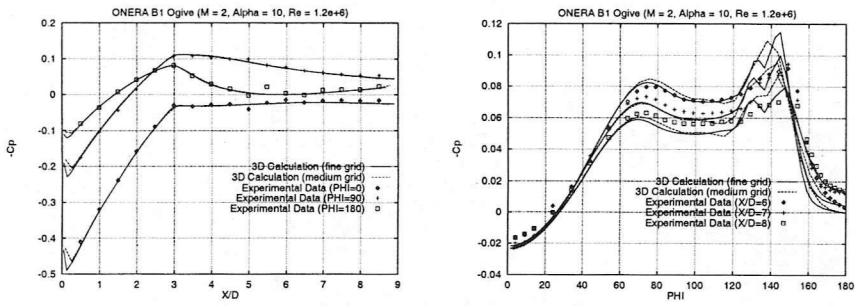

Figure 2: Pressure coefficient distributions
ONERA B1 Ogive, $M_\infty = 2$, $\alpha = 10^o$, Re = 0.16 10^6

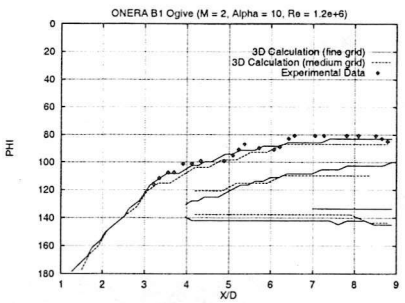

Figure 3: Separation line
ONERA B1 Ogive, $M_\infty = 2$, $\alpha = 10^o$, Re = 0.16 10^6

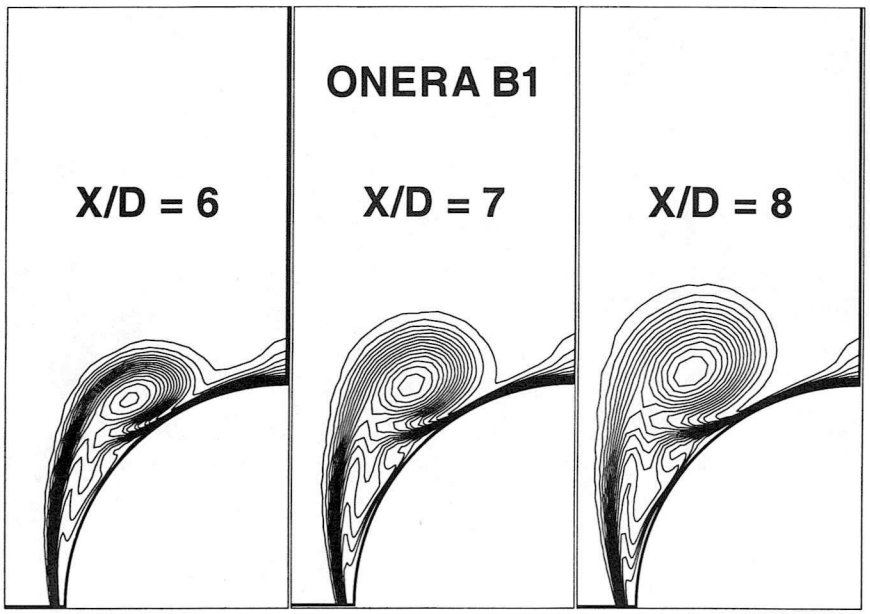

Figure 4: Stagnation pressure contours at different stations along the body
ONERA B1 Ogive, $M_\infty = 2$, $\alpha = 10^o$, Re = 0.16 10^6

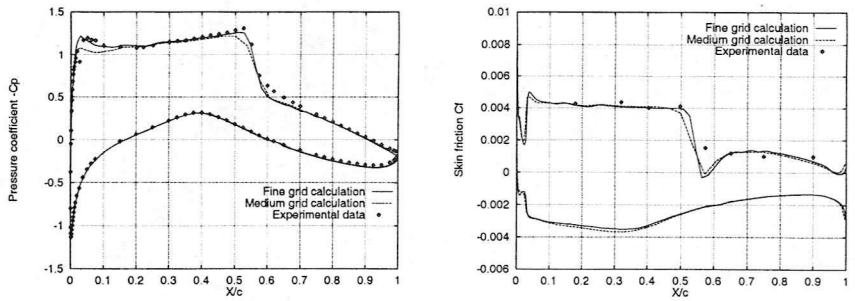

Figure 5: Pressure coefficient and skin friction distributions
RAE 2822 Infinite Wing, $M_\infty = 0.73$, $\alpha = 2.79^o$, Re = 6.5 10^6

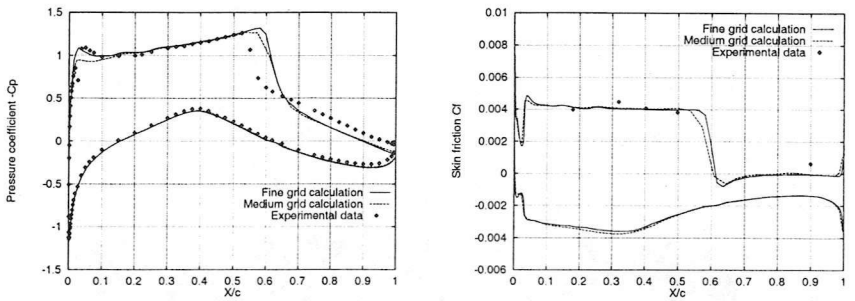

Figure 6: Pressure coefficient and skin friction distributions
RAE 2822 Infinite Wing, $M_\infty = 0.75$, $\alpha = 2.81^o$, Re = 6.2 10^6

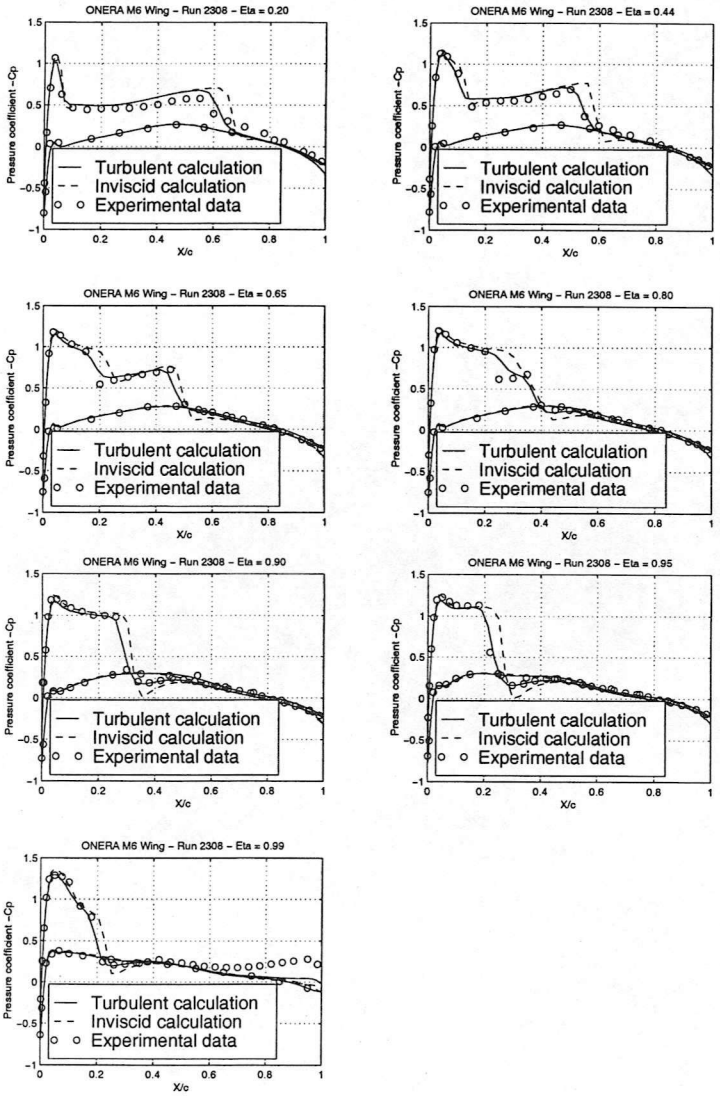

Figure 7: Pressure coefficient distribution
ONERA M6 Wing, $M_\infty = 0.84$, $\alpha = 3.06^o$, Re = 11.7 10^6

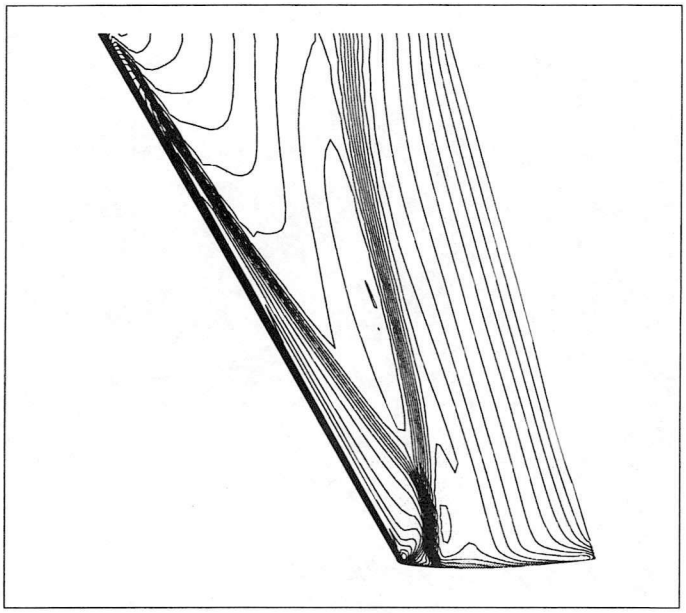

Figure 8: Pressure contours for the ONERA M6 Wing
$M_\infty = 0.84$, $\alpha = 3.06^o$, Re = 11.7 10^6

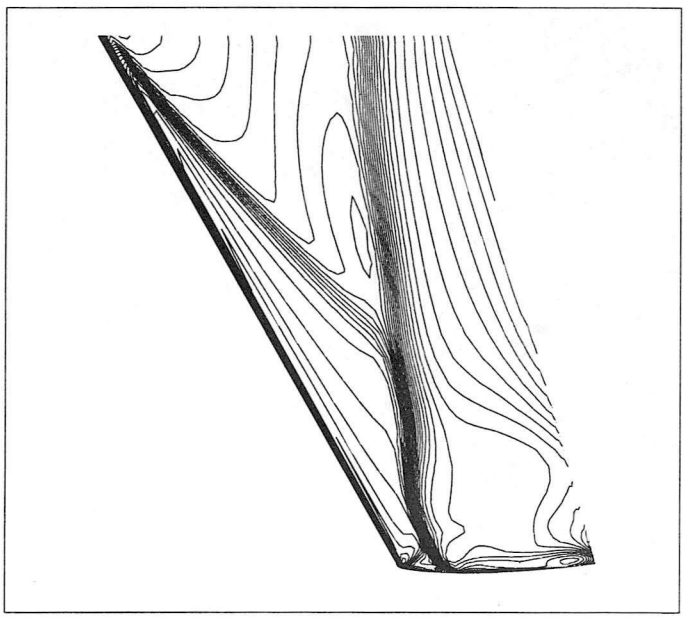

Figure 9: Pressure contours for the ONERA M6 Wing
$M_\infty = 0.84$, $\alpha = 6.06^o$, Re = 11.7 10^6

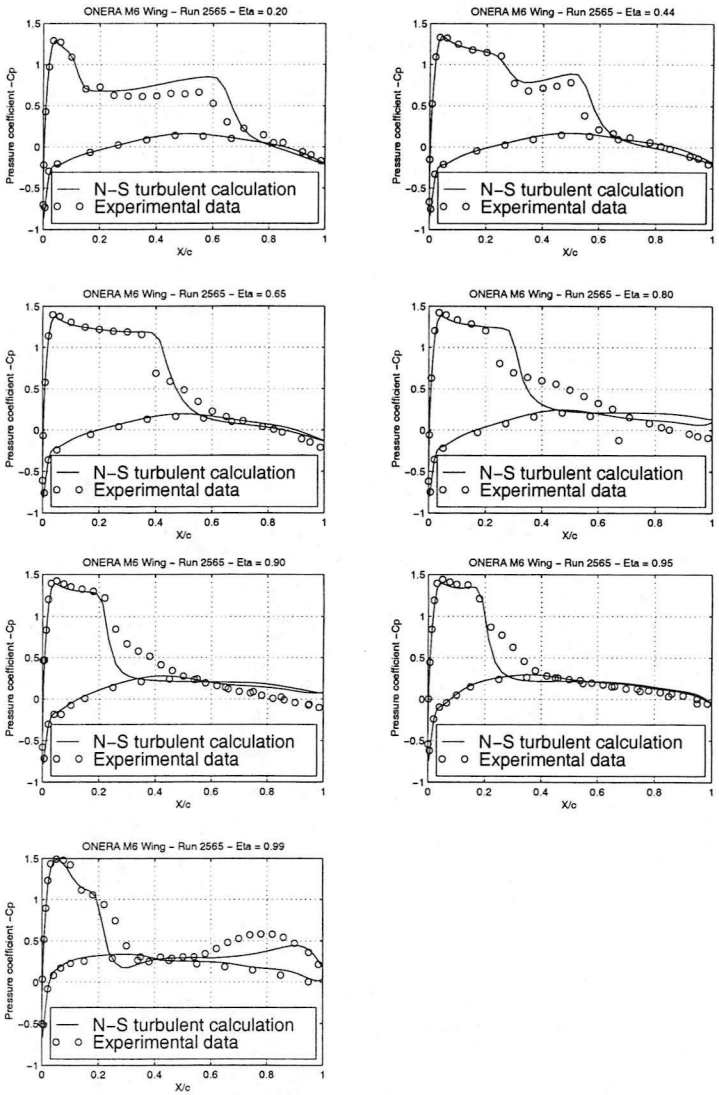

Figure 10: Pressure coefficient distribution
ONERA M6 Wing, $M_\infty = 0.84$, $\alpha = 6.06^o$, Re = 11.7 10^6

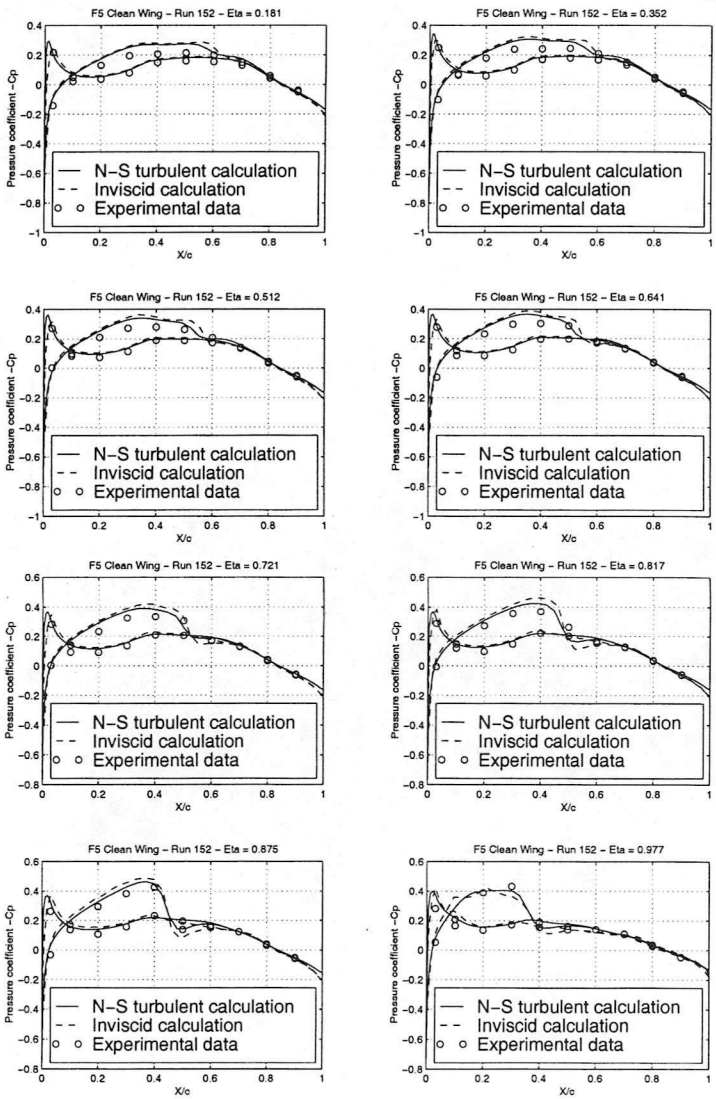

Figure 11: Pressure coefficient distribution
NLR-F5 Clean Wing, $M_\infty = 0.896$, $\alpha = 0.497^o$, Re = 5.79 10^6

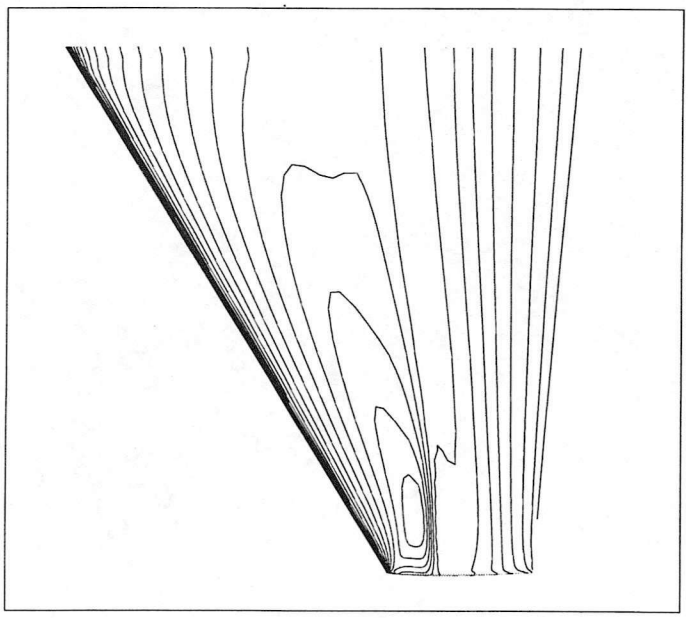

Figure 12: Pressure contours for the NLR-F5 Clean Wing
$M_\infty = 0.896$, $\alpha = 0.497^o$, Re = 5.79 10^6

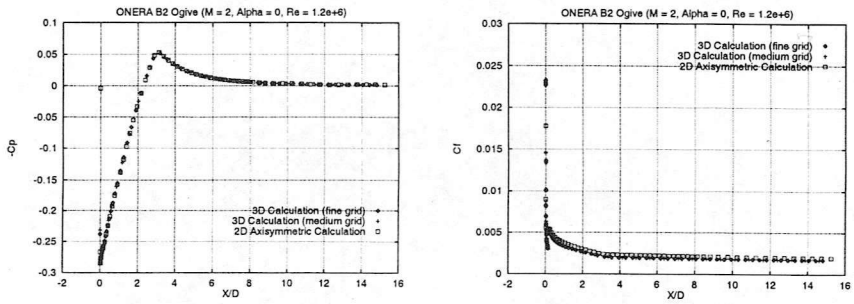

Figure 13: Pressure coefficient and skin friction distributions
ONERA B2 Ogive, $M_\infty = 2$, $\alpha = 0^o$, Re = 1.2 10^6

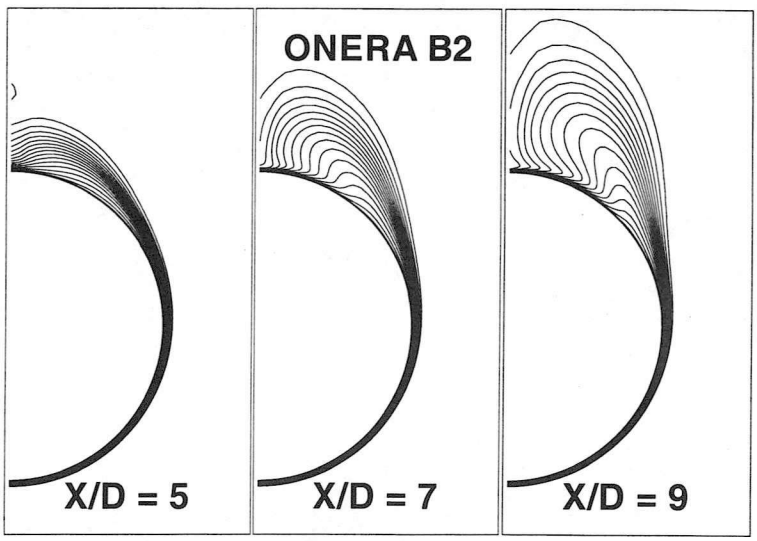

Figure 14: Stagnation pressure contours at different stations along the body
Standard Baldwin-Lomax turbulence model
ONERA B2 Ogive, $M_\infty = 2$, $\alpha = 10^o$, Re = 1.2 10^6

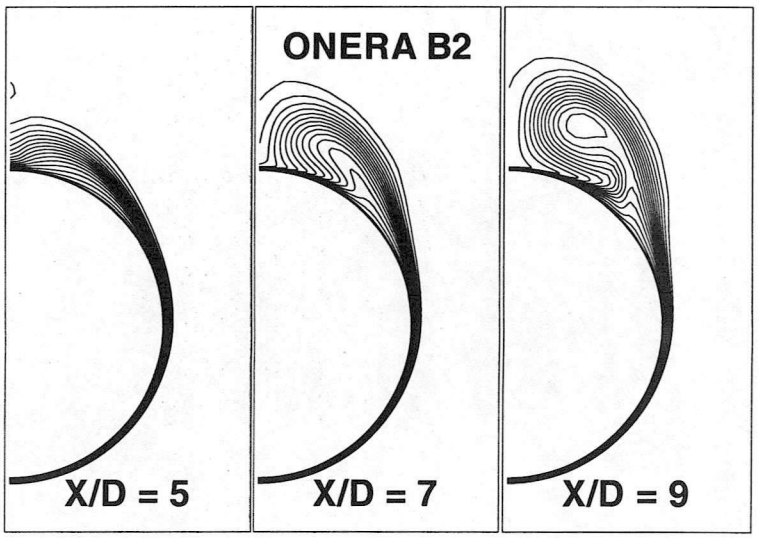

Figure 15: Stagnation pressure contours at different stations along the body
Baldwin-Lomax turbulence model + partial Degani-Schiff correction
ONERA B2 Ogive, $M_\infty = 2$, $\alpha = 10^o$, Re = 1.2 10^6